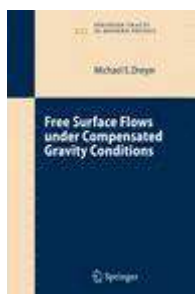


Book

Transmission Electron Microscopy of Semiconductor Nanostructures: Analysis of Composition and Strain State

Book Series Springer Tracts in Modern Physics
 Publisher Springer Berlin / Heidelberg
 ISSN 1615-0430
 Subject Physics and Astronomy
 Volume Volume 182/2003
 Copyright 2003
 Online Date Thursday, July 03, 2003

10 Chapters

Access to all content Access to some content Access to no content

<input type="checkbox"/>	Introduction		1-9
	Author	A. Rosenauer	
	Text	PDF (165 kb)	
<input type="checkbox"/>	Electron Diffraction		13-32
	Author	A. Rosenauer	
	Text	PDF (388 kb)	
<input type="checkbox"/>	Image Formation		33-53
	Author	A. Rosenauer	
	Text	PDF (896 kb)	
<input type="checkbox"/>	Strain State Analysis		57-85
	Author	A. Rosenauer	
	Text	PDF (1,745 kb)	
<input type="checkbox"/>	Lattice Fringe Analysis		87-136
	Author	A. Rosenauer	
	Text	PDF (2,278 kb)	
<input type="checkbox"/>	Introduction		139-145
	Author	A. Rosenauer	
	Text	PDF (193 kb)	
<input type="checkbox"/>	In _{0.6} Ga _{0.4} As/GaAs(001) SK Layers		147-167
	Author	A. Rosenauer	
	Text	PDF (1,134 kb)	
<input type="checkbox"/>	InAs Quantum Dots		169-192
	Author	A. Rosenauer	
	Text	PDF (1,206 kb)	

<input type="checkbox"/>	Electron Holography: AlAs/GaAs Superlattices	193-208
	Author	A. Rosenauer
	Text	PDF (787 kb)
<hr/>		
<input type="checkbox"/>	Outlook	209-210
	Author	A. Rosenauer
	Text	PDF (54 kb)

10 Chapters

Copyright ©2006, Springer. All Rights Reserved.

1 Introduction

The techniques described in this book are aimed at investigation of the properties of crystal with a spatial resolution that provides the view into the unit cell of the crystal. For this purpose, high-energy electrons are preferable, among all the different kinds of radiation that could be used. First, electrons possess a charge, and a beam of electrons can be focused in an inhomogeneous magnetic field, which allows the construction of an electromagnetic focusing lens. Among charged particles, electrons (and also positrons, but these are not useful here) possess the smallest mass, which minimizes the structural damage that they cause in the specimen. In the transmission electron microscope (TEM), electrons are accelerated to a few hundreds of keV. The de Broglie wavelength of the electrons is of the order of only a few picometers, and the point resolution of modern TEMs lies in the 0.1 nm range. In addition to the good spatial resolution, the strong interaction of the electrons with matter allows the interaction volume to be extremely small. One single column of only a few atoms is sufficient to determine the positions and, in principle, also the types of the atoms from the scattered electron wave.

The interaction of the electron beam with the specimen provides many channels of information that can be used for compositional analysis. First, the inelastic scattering of electrons can be used for energy-dispersive X-ray analysis (EDX), electron energy loss spectroscopy (EELS) and energy-filtered TEM (EFTEM) [1]. The spatial resolution, of the order of a few nanometers, is generally not sufficient to measure the composition of nanostructures with good accuracy. As an alternative, high-resolution TEM (HRTEM) can be utilized in combination with appropriate image evaluation techniques, where a resolution of the order of 0.2 nm can be achieved.

“Chemical lattice imaging” was introduced by Ourmazd and coworkers [2]; This allowed the chemical analysis of $\text{Al}_x\text{Ga}_{1-x}\text{As}$ heterostructures on an atomic scale. Another example of an evaluation method related to HRTEM is the QUANTITEM (quantitative analysis of information from transmission electron micrographs) procedure which yields the projected potential of the samples for crystals such as Si and Ge when only two Bloch waves are strongly excited [3, 4, 5]. An alternative method, by Stenkamp and Jäger [6], uses systematic variations of the image contrast pattern to obtain the local

composition of SiGe alloys for certain ranges of objective lens defocus Δf and specimen thickness t by measuring local Fourier coefficients.

This book focuses on two methods to quantify the information contained in HRTEM images that are particularly useful for the investigation of semiconductor heteroepitaxial layers, where the strain state and the composition on an atomic scale are of interest: strain state analysis, and composition evaluation by lattice fringe analysis (CELFA).

1.1 Strain State Analysis [7, 8, 9, 10]

The basis of one possible approach to the problem of determining strain and composition on an atomic scale is the measurement of local lattice parameters, i.e. the measurement of distances between adjacent atomic columns. This approach is based principally on an important result of channeling theory: presupposing an electron beam parallel to a zone axis of the specimen, Van Dyck et al. showed [11] that the positions of the atomic columns are given by the local intensity maxima of the electron wave function at the object exit surface. If the objective lens introduces only radially symmetric aberrations, this relation holds even in the image plane for perfect-crystal specimens. Nevertheless, the objective lens aberrations give rise to delocalization. The information content of each point of the wave function at the object exit surface is spread over an area in the image plane whose size depends on the lens aberrations and defocus. Consequently, sharp interfaces appear blurred in the image. These effects can be minimized by using the proper defocus. Although errors have to be expected close to chemical transitions in the specimen and in regions where the specimen thickness changes rapidly, the positions of maximum image intensity are well suited for the measurement of local lattice parameter variations and of displacements of atomic columns with good accuracy. For this purpose, only a sufficiently constant relationship needs to be assumed between the positions of the atomic columns and the positions of the intensity maxima, whereas the relationship itself does not need to be known at all.

The impact of objective lens aberrations can be avoided by the reconstruction of the aberration-free exit wave function, which can be achieved by two different approaches. In one of these approaches, a Möllenstedt biprism is inserted close to the first intermediate image plane to perform off-axis electron holography [12, 13]. In the other approach, a series of HRTEM images taken at systematically varied defocus values is used in the focal-variation reconstruction method published by Coene et al. [14].

The local composition can be extracted from a single HRTEM image or, more accurately, from the amplitude of the reconstructed electron exit wave function, if the relationship between the composition and the lattice parameter is known. For many compound semiconductors, e.g. $\text{In}_x\text{Ga}_{1-x}\text{As}$ and $\text{Cd}_x\text{Zn}_{1-x}\text{Se}$, Vegard's law,

$$a_{A_xB_{1-x}C} = a_{BC} + x(a_{AC} - a_{BC}), \quad (1.1)$$

can be applied; here the lattice parameter and the composition are linearly correlated. If a mismatch exists between the lattice parameters of the substrate and the epilayer, the distortion of the unit cells in the epilayer must be taken into account. The tetragonal distortion can be easily calculated for coherently strained two-dimensional layers below the critical thickness [15] for plastic relaxation by misfit dislocations.

Measurement of local lattice parameters was applied by Bierwolf et al. [16] and Jouneau et al. [17] to investigate the strain distribution of thin epitaxial layers. Robertson et al. [18] used Fourier-filtered HRTEM images to measure the spacings and cumulative deviations of lattice fringes. Hÿtch et al. [19, 20, 21] used a Fourier filtering technique to derive the geometric local phase of reflections in the Fourier-transformed image (diffractogram).

The situation becomes more difficult for three-dimensional growth modes. Deviations from a tetragonal distortion occur close to the surface owing to the elastic relaxation of the strained lattice. The finite-element method (FEM) was first applied to compute the strain distribution in nanoscale islands in the SiGe/Si(001) by Christiansen et al. [22]. A complete relaxation of the misfit strain close to the island surface was obtained; this is regarded as the major driving force for the island growth. Therefore, an accurate knowledge of the strain distribution is a necessary prerequisite for composition evaluation from local lattice parameters in the case of epitaxial islands.

Another question to be addressed is the elastic relaxation of strained structures due to the small thickness of an HRTEM specimen (typically 20 nm), which can significantly modify the tetragonal distortion, depending on the local specimen thickness and the dimensions of the strained structure. The specimen thickness must be accurately measured in the region of interest of the HRTEM image that is being analyzed. A further important step in the quantification is the calculation of the elastic relaxation as a function of the thickness of the TEM specimen and the layer morphology. Analytical solutions to this problem for simple layer morphologies have been presented by Treacy et al. [23]. For more complicated morphologies, FEM simulations can be applied [24].

1.2 CELFA [7, 25, 26, 27, 28]

Owing to the modification of local lattice parameters by the local specimen thickness and by elastic strain relaxation in islands, a different and less elaborate approach to composition determination is desirable. In this book, an alternative method is described that exploits chemically sensitive reflections such as the {002} reflections available in sphalerite-type crystals. This type of reflection provides an amplitude that depends strongly on the crystal composition but often is rather small, as in $\text{In}_x\text{Ga}_{1-x}\text{As}$ and $\text{Cd}_x\text{Zn}_{1-x}\text{Se}$, for example.

Single-beam dark-field imaging with a chemically sensitive reflection is conventionally used to display variations of the chemical composition qualitatively. Since the local image intensity is proportional to the square of the amplitude of the chemically sensitive reflection, quantitative data can be extracted, in principle. However, several problems exist. The signal-to-noise ratio is typically small, owing to the small amplitude of the chemically sensitive reflection and to inelastic scattering. Another significant disadvantage may be explained as follows. The structure amplitude of a chemically sensitive reflection depends linearly on the elemental concentration x in a semiconductor $A_xB_{1-x}C$. Depending on the atomic scattering factors of the atoms involved, the sign of the structure amplitude may change at a certain concentration x_0 . As a consequence, the amplitudes of the chemically sensitive beam are similar at values of x equal to $x_0 \pm \delta x$ whereas the phases differ by π . It is a disadvantage of the single-beam dark-field imaging technique that the phase of the beam is lost, but is essential to resolve the ambiguity described above.

The CELFA technique leads to a significantly improved signal-to-noise ratio and recovers the phase information contained in the chemically sensitive beam. The technique exploits a two- or three-beam interference of the chemically sensitive beam with the undiffracted beam. A three-beam condition using an additional, third reflection can be used to obtain information about the local specimen thickness. An off-axis imaging condition is used to enlarge the extinction distance, which minimizes the influence of specimen thickness variations. A particularly elegant way to obtain the amplitude and phase of the chemically sensitive beam, as well as the local specimen thickness, is off-axis electron holography, where the chemically sensitive reflection interferes with a reference beam that is spatially homogeneous. The specimen thickness is evaluated from the phase of the central beam of the centered sideband of the electron hologram.

The methods described above have been applied to a variety of material systems, including $\text{In}_x\text{Ga}_{1-x}\text{As}$ [7, 24, 29, 30, 31, 32, 33, 34], $\text{Cd}_x\text{Zn}_{1-x}\text{Se}$ [7, 35, 36, 37, 38, 39, 40, 41, 42, 43, 44, 45, 46, 47, 48, 49, 50, 51, 52], $\text{Al}_x\text{Ga}_{1-x}\text{As}$ [25, 53, 54], $\text{Al}_x\text{Ga}_{1-x}\text{N}$ [55, 56] and $\text{In}_x\text{Ga}_{1-x}\text{N}$ [57, 58, 59, 60]. A discussion of all these applications clearly goes beyond the scope of this book. Therefore, the presentation of applications will be restricted to investigations of $\text{In}_x\text{Ga}_{1-x}\text{As}$ Stranski-Krastanov (SK) layers and composition determination of $\text{Al}_x\text{Ga}_{1-x}\text{As}$ / GaAs superlattices by off-axis electron holography.

1.3 Organization of the Book

The present book is organized in the following way. The first part provides the theoretical fundamentals of transmission electron microscopy needed in the second part, which focuses on a description of strain state analysis and on the composition evaluation by lattice fringe analysis techniques. In the third

part, we describe the application of these techniques to the investigation of low-dimensional semiconductor heterostructures such as $\text{In}_x\text{Ga}_{1-x}\text{As}$ SK layers.

In Part I of this book, we describe the electron wave on its way from the specimen surface to the image. Chapter 2 starts with the interaction of the electron wave with a crystalline specimen. First, we treat the scattering by a single atom in Sect. 2.1. Section 2.2 describes the effect of electron diffraction in the kinematical approximation, which is valid for crystals with a thickness of only a few nanometers in the direction of the electron beam. More realistic specimen thicknesses are treated in Sect. 2.3 within the framework of the Bloch wave approach. Finally, channeling theory is used in Sect. 2.4 to show that the positions of maximum intensity of the wave function at the object exit surface correspond to the positions of atomic columns, presupposing an exact zone axis orientation of the specimen.

Chapter 3 is concerned with the intensity pattern observed in the image plane. It starts with the fictitious assumption of an ideal microscope and then allows for spherical aberration and defocus in Sect. 3.1. Effects of incoherence such as fluctuations of the high tension or objective lens current are treated in Sect. 3.2. At the end of Chap. 3, two approaches are described in Sect. 3.3 that allow the reconstruction of the wave function at the object exit surface: the focal-variation technique and off-axis electron holography.

Part II deals with the methods that have been developed for digital image analysis. The first procedure, discussed in Chap. 4, is strain state analysis. Section 4.1 outlines the measurement of the displacements and spacings of lattice positions. A knowledge of the local specimen thickness is an important prerequisite because the tetragonal distortion in a thin TEM specimen is reduced in comparison with a bulk sample. Section 4.2 outlines a procedure to measure the thickness, based upon QUANTITEM. After that, Sect. 4.3 focuses on the determination of the elastic relaxation of a thin specimen by FEM simulations.

A rather detailed description of the CELFA technique is presented in Chap. 5. The basic ideas behind CELFA are introduced in Sect. 5.1. Subsequently, Sect. 5.2 gives a theoretical treatment of the technique. Practical considerations follow in Sect. 5.3, which is concerned with the actual procedures for the measurement of amplitudes and phases of reflections, as well as with the errors in the evaluated composition due to objective lens aberrations and specimen thickness uncertainties. The effect of strain is addressed in Sect. 5.4 and, finally, the impact of a nonrandom distribution of atom types that share the same crystal sublattice is discussed in Sect. 5.5.

Applications of the evaluation methods are given in Part III. Chapter 6 introduces the Stranski-Krastanov growth mode (Sect. 6.1) and gives a survey of the present level of understanding of segregation effects in III-V ternary alloys (Sect. 6.2). Chapter 7 outlines the investigations of $\text{In}_{0.6}\text{Ga}_{0.4}\text{As}$ SK layers. It shows how the application of strain state analysis and the CELFA tech-

nique allows novel insights into the morphology of free-standing and capped SK layers. The investigations reveal that effects such as strain-induced migration of Ga and In, segregation, and incorporation of migrating In into the growing cap layer lead to a considerable morphological transformation of the SK layer during overgrowth of GaAs.

The effect of segregation leads to interesting and surprising morphologies of the wetting layer and islands as has been shown by the investigation of nominally binary InAs quantum dots presented in Chap. 8. Here we have found that the putative binary islands contained more than 50% Ga. An investigation of the wetting layers revealed, in a very clear and unambiguous manner, the existence of segregation. This observation is in contradiction to the wide-spread assumption that segregation is based upon an exchange reaction of In and Ga at the growth surface.

Chapter 9 makes the point that electron holography could be very useful for measuring the composition of materials in cases where the specimen thickness is of crucial importance in chemical analysis. Here we show that the measurement of the local phase of the (000) beam of the centered sideband, combined with the amplitude of the chemically sensitive (002) beam, allows one to deduce both the specimen thickness and the composition, in an iterative and self-consistent way. Although accurate values of the mean inner potential are generally not available at present, the suggested method leads to good accuracy in the measured composition. Here we describe the application of the method to an AlAs/GaAs superlattice, where again the effect of segregation is demonstrated and its efficiency is measured.

References

1. W. Grogger, F. Hofer, P. Warbichler, G. Kothleitner: *Microsc. Microanal.* **6**, 161 (2000) [1](#)
2. A. Ourmazd, D.W. Taylor, J. Cunningham, C.W. Tu: *Phys. Rev. Lett.* **62**, 933 (1989) [1](#)
3. C. Kisielowski, P. Schwander, F.H. Baumann, M. Seibt, Y.O. Kim, A. Ourmazd: *Ultramicroscopy* **58**, 131 (1995) [1](#)
4. A. Ourmazd, P. Schwander, C. Kisielowski, M. Seibt, F.H. Baumann, Y.O. Kim: *Inst. Phys. Conf. Ser.* **134**: Section 1, 1 (1993) [1](#)
5. J.-L. Maurice, P. Schwander, F.H. Baumann, A. Ourmazd: *Ultramicroscopy* **68**, 149 (1997) [1](#)
6. D. Stenkamp, W. Jäger: *Ultramicroscopy* **50**, 321 (1993) [1](#)
7. A. Rosenauer, D. Gerthsen: *Adv. Imaging Electron Phys.* **107**, 121 (1999) [2](#), [3](#), [4](#)
8. A. Rosenauer, T. Remmele, U. Fischer, A. Förster, D. Gerthsen: "Strain determination in mismatched semiconductor heterostructures by the digital analysis of lattice images". In: *Microscopy of Semiconducting Materials 1997*, Oxford, UK, April 7–10, 1997, Proceedings of the Royal Microscopical Society Conference, ed. by A.G. Cullis, J.L. Hutchison (Institute of Physics, Bristol, 1997) pp. 39–42 [2](#)

9. A. Rosenauer, T. Remmele, D. Gerthsen, K. Tillmann, A. Förster: *Optik* **105**, 99 (1997) [2](#)
10. A. Rosenauer, S. Kaiser, T. Reisinger, J. Zweck, W. Gebhardt, D. Gerthsen: *Optik* **102**, 63 (1996) [2](#)
11. D. Van Dyck, M. Op de Beeck: *Ultramicroscopy* **64**, 99 (1996) [2](#)
12. H. Lichte: *Ultramicroscopy* **47**, 223 (1992) [2](#)
13. H. Lichte, E. Völkl: *Ultramicroscopy* **47**, 231 (1992) [2](#)
14. W.M.J. Coene, A. Thust, M. Op de Beeck, D. Van Dyck: *Ultramicroscopy* **64**, 109 (1996) [2](#)
15. R. Hull, J.C. Bean: *Critical Reviews in Solid State and Materials Sciences* **17**, 507 (1992) [3](#)
16. R. Bierwolf, M. Hohenstein, F. Phillipp, O. Brandt, G.E. Crook, K. Ploog: *Ultramicroscopy* **49**, 273 (1993) [3](#)
17. P.H. Jouneau, A. Tardot, G. Feulliet, H. Marietta, J. Cibert: *J. Appl. Phys.* **75**, 7310 (1994) [3](#)
18. M.D. Robertson, J.E. Curie, J.M. Corbett, J.B. Webb: *Ultramicroscopy* **58**, 175 (1995) [3](#)
19. M.J. Hytch, L. Potez: *Phil. Mag. A* **76**, 1119 (1997) [3](#)
20. M.J. Hytch: *Microsc. Microanal. Microstruct.* **8**, 41 (1997) [3](#)
21. M.J. Hytch, E. Snoeck, R. Kilaas: *Ultramicroscopy* **74**, 131 (1998) [3](#)
22. S. Christiansen, M. Albrecht, H.P. Strunk, H.J. Maier: *Appl. Phys. Lett.* **64**, 3617 (1994) [3](#)
23. M.M.J. Treacy, J.M. Gibson: *J. Vac. Sci. Technol. B* **4**, 1458 (1986) [3](#)
24. K. Tillmann, A. Thust, M. Lentzen, P. Swiatek, A. Förster, K. Urban, D. Gerthsen, T. Remmele, A. Rosenauer: *Phil. Mag. Lett.* **74**, 309 (1996) [3](#), [4](#)
25. A. Rosenauer, D. Van Dyck, M. Arzberger, G. Abstreiter: *Ultramicroscopy* **88**, 51 (2001) [3](#), [4](#)
26. A. Rosenauer, D. Van Dyck: "The effect of strain on the chemically sensitive imaging with the (002) reflection in sphalerite type crystals". In: *Proceedings of EUREM 12*, Brno, Czech Republic, July 9–14, 2000, p. I121 [3](#)
27. A. Rosenauer, D. Gerthsen: *Ultramicroscopy* **76**, 49 (1999) [3](#)
28. A. Rosenauer, U. Fischer, D. Gerthsen, A. Förster: *Ultramicroscopy* **72**, 121 (1998) [3](#)
29. A. Rosenauer, D. Gerthsen, D. Van Dyck, M. Arzberger, G. Böhm, G. Abstreiter: *Phys. Rev. B* **64**, 245334-1 (2001) [4](#)
30. A. Rosenauer, W. Oberst, D. Litvinov, D. Gerthsen, A. Foerster, R. Schmidt: *Phys. Rev. B* **61**, 8276 (2000) [4](#)
31. A.F. Tsatsulnikov, B.V. Volovik, N.N. Ledentsov, M.V. Maximov, A.Yu. Egorov, A.R. Kovsh, V.M. Ustinov, A.E. Zhukov, P.S. Kopev, Z.I. Alferov, I.A. Kozin, M.V. Belousov, I.P. Soshnikov, P. Werner, D. Litvinov, U. Fischer, A. Rosenauer, D. Gerthsen: *J. Electron. Mater.* **28**, 537 (1999) [4](#)
32. A. Rosenauer, W. Oberst, D. Gerthsen, A. Förster: *Thin Solid Films* **357**, 18 (1999) [4](#)
33. A. Rosenauer, U. Fischer, D. Gerthsen, A. Förster: *Appl. Phys. Lett.* **71**, 3868 (1997) [4](#)
34. U. Woggon, W. Langbein, J.M. Hvam, A. Rosenauer, T. Remmele, D. Gerthsen: *Appl. Phys. Lett.* **71**, 377 (1997) [4](#)

35. M. Strassburg, T. Deniozou, A. Hoffmann, S. Rodt, V. Turck, R. Heitz, U.W. Pohl, D. Bimberg, D. Litvinov, A. Rosenauer, D. Gerthsen, S. Schwedhelm, I. Kudryashov, K. Lischka, D. Schikora: *J. Cryst. Growth* **214–215**, 756 (2000) [4](#)
36. D. Gerthsen, A. Rosenauer, D. Litvinov, N. Peranio: *J. Cryst. Growth* **214–215**, 707 (2000) [4](#)
37. D. Schikora, S. Schwedhelm, I. Kudryashov, K. Lischka, D. Litvinov, A. Rosenauer, D. Gerthsen, A. Strassburg, A. Hoffmann, D. Bimberg: *J. Cryst. Growth* **214–215**, 698 (2000) [4](#)
38. M. Strassburg, M. Dworzak, A. Hoffmann, R. Heitz, U.W. Pohl, D. Bimberg, D. Litvinov, A. Rosenauer, D. Gerthsen, I. Kudryashov, K. Lischka, D. Schikora: *Phys. Status Solidi A* **180**, 281 (2000) [4](#)
39. N.N. Ledentsov, I.L. Krestnikov, M. Strassburg, R. Engelhardt, S. Rodt, R. Heitz, U.W. Pohl, A. Hoffmann, D. Bimberg, A.V. Sakharov, W.V. Lundin, A.S. Usikov, Z.I. Alferov, D. Litvinov, A. Rosenauer, D. Gerthsen: *Thin Solid Films* **367**, 40 (2000) [4](#)
40. D. Litvinov, A. Rosenauer, D. Gerthsen, N.N. Ledentsov: *Phys. Rev. B* **61**, 16819 (2000) [4](#)
41. N. Peranio, A. Rosenauer, D. Gerthsen, S.V. Sorokin, I.V. Sedova, S.V. Ivanov: *Phys. Rev. B* **61**, 16015 (2000) [4](#)
42. M. Strassburg, T. Deniozou, A. Hoffmann, R. Heitz, U.W. Pohl, D. Bimberg, D. Litvinov, A. Rosenauer, D. Gerthsen, S. Schwedhelm, K. Lischka, D. Schikora: *Appl. Phys. Lett.* **76**, 685 (2000) [4](#)
43. D. Schikora, S. Schwedhelm, D.J. As, K. Lischka, D. Litvinov, A. Rosenauer, D. Gerthsen, M. Strassburg, A. Hoffmann, D. Bimberg: *Appl. Phys. Lett.* **76**, 418 (2000) [4](#)
44. A. Rosenauer, N. Peranio, D. Gerthsen: “Investigation of CdSe/ZnSe quantum dot structures by composition evaluation by lattice fringe analysis”. In: *Microscopy of Semiconducting Materials 1999*, Oxford, UK, March 22–25, 1999, Proceedings of the Institute of Physics Conference, Institute of Physics Conference Series Number 164, ed. by A.G. Cullis, J.L. Hutchison, (Institute of Physics, Bristol, 1997) [4](#)
45. R. Engelhardt, U.W. Pohl, D. Bimberg, D. Litvinov, A. Rosenauer, D. Gerthsen: *J. Appl. Phys.* **86**, 5578 (1999) [4](#)
46. I.L. Krestnikov, M. Strassburg, M. Caesar, A. Hoffmann, U.W. Pohl, D. Bimberg, N.N. Ledentsov, P.S. Kopev, Zh.I. Alferov, D. Litvinov, A. Rosenauer, D. Gerthsen: *Phys. Rev. B* **60**, 8695 (1999) [4](#)
47. M. Strassburg, R. Heitz, V. Turck, S. Rodt, U.W. Pohl, A. Hoffmann, D. Bimberg, I.L. Krestnikov, V.A. Shchuxin, N.N. Ledentsov, Z.I. Alferov, D. Litvinov, A. Rosenauer, D. Gerthsen: *J. Electron. Mater.* **28**, 506 (1999) [4](#)
48. K.G. Chinyama, K.P. O’Donnell, A. Rosenauer, D. Gerthsen: *J. Cryst. Growth* **203**, 362 (1999) [4](#)
49. I.L. Krestnikov, S.V. Ivanov, P.S. Kopev, N.N. Ledentsov, M.V. Maximov, A.V. Sakharov, S.V. Sorokin, A. Rosenauer, D. Gerthsen, C.M. Sotomayor-Torres, D. Bimberg, Zh.I. Alferov: *Mater. Sci. Eng. B* **51**, 26 (1998) [4](#)
50. M. Strassburg, A.V. Kutzer, U.W. Pohl, A. Hoffmann, I. Broser, N.N. Ledentsov, D. Bimberg, A. Rosenauer, U. Fischer, D. Gerthsen, I.L. Krestnikov, M.V. Maximov, C.O. Kop: *Appl. Phys. Lett.* **72**, 942 (1998) [4](#)

51. T. Reisinger, S. Lankes, M.J. Kastner, A. Rosenauer, F. Franzen, M. Meier, W. Gebhardt: *J. Cryst. Growth* **159**, 510 (1996) 4
52. A. Rosenauer, T. Reisinger, E. Steinkirchner, J. Zweck, W. Gebhardt: *J. Cryst. Growth* **152**, 42 (1995) 4
53. E. Schomburg, S. Brandl, S. Winnerl, K.F. Renk, N.N. Ledentsov, V.M. Ustinov, A. Zhukov, P.S. Kopev, H.W. Hubers, J. Schubert, H.P. Roser, A. Rosenauer, D. Litvinov, D. Gerthsen, J.M. Chamberlain: *Physica E* **7**, 814 (2000) 4
54. E. Schomburg, S. Brandl, K.F. Renk, N.N. Ledentsov, V.M. Ustinov, A.E. Zhukov, A.R. Kovsh, A.Yu. Egorov, R.N. Kyutt, B.V. Volovik, P.S. Kopev, Zh.I. Alferov, A. Rosenauer, D. Litvinov, D. Gerthsen, D.G. Pavelev, Y.I. Koschurinov: *Phys. Lett. A* **262**, 396 (1999) 4
55. B. Neubauer, A. Rosenauer, D. Gerthsen, O. Ambacher, M. Stutzmann, M. Albrecht, H.P. Strunk: *Mater. Sci. Eng. B* **59**, 182 (1999) 4
56. B. Neubauer, A. Rosenauer, D. Gerthsen, O. Ambacher, M. Stutzmann: *Appl. Phys. Lett.* **73**, 930 (1998) 4
57. D. Gerthsen, E. Hahn, B. Neubauer, A. Rosenauer, O. Schön, M. Heuken: *Phys. Status Solidi A* **177**, 145 (2000) 4
58. I.P. Soshnikov, V.V. Lundin, A.S. Usikov, I.P. Kalmykova, N.N. Ledentsov, A. Rosenauer, B. Neubauer, D. Gerthsen: *Semiconductors* **34**, 621 (2000) 4
59. B. Neubauer, H. Widmann, D. Gerthsen, T. Stephan, H. Kalt, J. Bläsing, P. Veit, A. Krost, O. Schön, M. Heuken: "Structural properties, In distribution and photoluminescence of multiple InGa_N/Ga_N quantum well structures". In: *Proceedings of International Workshop on Nitride Semiconductors*, Nagoya, (Institute of Pure and Applied Physics, Tokyo, 2000) vol. 1002, p. 375 4
60. D. Gerthsen, B. Neubauer, A. Rosenauer, T. Stephan, H. Kalt, O. Schön, M. Heuken: *Appl. Phys. Lett.* **79**, 2552 (2001) 4

2 Electron Diffraction

This chapter describes the elastic Coulomb interaction of an incident electron wave with a crystalline specimen. We start with the scattering of the electron wave function of the incident electrons by a single atom. The integral form of the Schrödinger equation results in a recursive description of the scattered electron wave function Ψ_S as a Born series. The scattered electron wave is calculated in the first Born approximation, and we find that the atomic scattering amplitude for electrons quickly decreases with increasing scattering angle. The periodic arrangement of atoms in the crystalline specimen together with electron scattering leads to electron diffraction. The structure amplitude of the crystal unit cell is used to describe the diffraction of electrons by a thin-foil specimen. This kinematical approximation reveals the origin of the chemically sensitive beams that constitute the basis of composition evaluation by the CELFA method. Dynamical effects of electron diffraction are taken into account using the Bloch wave formalism. With respect to the CELFA technique, we discuss the dependence of the beams on the specimen thickness and show how this dependence can be influenced by varying the excitation condition. Finally, we set out the basis of strain state analysis by discussing the correlation between the atomic positions and the positions of maximum image intensity that appear in the amplitude “image” of the wave function at the exit surface of the object in the framework of channeling theory. Further information about the topics discussed in this chapter may be found in [1, 2, 3].

2.1 Single-Atom Electron Scattering

2.1.1 The Integral Form of the Schrödinger Equation

We start our brief outline of diffraction theory with the scattering of an electron by a single atom that is tightly bound in a crystal. We consider only the case of elastic scattering, where momentum and energy are conserved. Owing to the large difference between the masses of the electron and the crystal, the energy transfer from the electron to the crystal is negligible and the electron wavelength does not change in the scattering process. The problem can be described by the stationary

Schrödinger equation

$$\nabla^2 \Psi(\mathbf{r}) + \frac{8\pi^2 m e}{h^2} (E + \Phi(\mathbf{r})) \Psi(\mathbf{r}) = 0, \quad (2.1)$$

where E and m are the relativistically corrected values of the accelerating potential and of the mass of the incident electron, respectively, $\Phi(\mathbf{r})$ is the Coulomb potential of the scattering atom, e is the elementary charge, and h is Planck's constant. Even in an electron microscope operating at only 100 keV, the electrons travel at over half the speed of light. It is thus clear that relativistic corrections must be taken into account. The relativistic corrections involved in (2.1) are

$$\begin{aligned} E &= U \left(1 + \frac{eU}{2m_0 c^2} \right), \\ m &= m_0 \sqrt{\left(1 + \frac{h^2}{m_0^2 c^2 \lambda^2} \right)}, \\ \lambda &= \frac{h}{\sqrt{2m_0 eU (1 + eU/2m_0 c^2)}}, \end{aligned} \quad (2.2)$$

where U is the accelerating voltage, λ the de Broglie wavelength, m_0 the rest mass of the incident electron and c the speed of light in vacuum. Equation (2.1) can be interpreted as an inhomogeneous differential equation with an inhomogeneity

$$f(\mathbf{r}) := -\frac{8\pi^2 m e}{h^2} \Phi(\mathbf{r}) \Psi(\mathbf{r}). \quad (2.3)$$

Using the abbreviation

$$k'^2 := \frac{2m e}{h^2} E \quad (2.4)$$

and defining the linear differential operator

$$\mathbb{L} := \left[\nabla^2 + 4\pi^2 k'^2 \right], \quad (2.5)$$

we can obtain a Green's function

$$G(\mathbf{r} - \mathbf{r}') = -\frac{1}{4\pi} \frac{\exp(-2\pi i k' |\mathbf{r} - \mathbf{r}'|)}{|\mathbf{r} - \mathbf{r}'|}, \quad (2.6)$$

which obeys

$$\mathbb{L} G(\mathbf{r} - \mathbf{r}') = \delta(\mathbf{r} - \mathbf{r}'), \quad (2.7)$$

where δ is Dirac's delta "function"¹ (Sect. B.3). A solution of the inhomogeneous differential equation

¹ Equation (2.7) can easily be proven using the relation $\nabla^2(1/|\mathbf{r} - \mathbf{r}'|) = -4\pi\delta(\mathbf{r} - \mathbf{r}')$.

$$\mathbb{L}\Psi(\mathbf{r}) = f(\mathbf{r}) \quad (2.8)$$

is given by

$$\Psi(\mathbf{r}) = \Psi_0(\mathbf{r}) + \int_{\Omega} G(\mathbf{r} - \mathbf{r}') f(\mathbf{r}') d^3\mathbf{r}' , \quad (2.9)$$

where Ω is the scattering volume. Inserting $G(\mathbf{r} - \mathbf{r}')$ from (2.6), we finally obtain

$$\boxed{\Psi(\mathbf{r}) = \Psi_0(\mathbf{r}) + \frac{2\pi me}{h^2} \int_{\Omega} \frac{\exp(-2\pi i k' |\mathbf{r} - \mathbf{r}'|)}{|\mathbf{r} - \mathbf{r}'|} \Phi(\mathbf{r}') \Psi(\mathbf{r}') d^3\mathbf{r}' ,} \quad (2.10)$$

where $\Psi_0(\mathbf{r})$ is a solution of the homogeneous differential equation (2.7). An expression for this solution can be obtained from the condition that $\Psi(\mathbf{r}) = \Psi_0(\mathbf{r})$ for $\Phi(\mathbf{r}) = 0$. Thus, $\Psi_0(\mathbf{r})$ is the incident electron wave

$$\Psi_0(\mathbf{r}) = \exp(-2\pi i \mathbf{k}_0 \cdot \mathbf{r}) , \quad (2.11)$$

with a wave vector \mathbf{k}_0 .

2.1.2 The Atomic Scattering Amplitude for Electrons

Using (2.10), $\Psi(\mathbf{r})$ can be expressed as a Born series

$$\Psi(\mathbf{r}) = \sum_{n=0}^{\infty} \Psi_n(\mathbf{r}) , \quad (2.12)$$

where $\Psi_n(\mathbf{r})$ is obtained from the integral (2.10) by putting $\Psi(\mathbf{r}) = \Psi_{n-1}(\mathbf{r})$. In the first Born approximation we obtain

$$\Psi_1(\mathbf{r}) = \sigma \int_{\Omega} \frac{\exp(-2\pi i k' |\mathbf{r} - \mathbf{r}'|)}{|\mathbf{r} - \mathbf{r}'|} \Phi(\mathbf{r}') \exp(-2\pi i \mathbf{k}_0 \cdot \mathbf{r}') d^3\mathbf{r}' , \quad (2.13)$$

where σ is the interaction constant, given by

$$\sigma = \frac{2\pi me}{h^2} . \quad (2.14)$$

In the following, we consider $\Psi(\mathbf{r})$ only for $|\mathbf{r}'| \ll |\mathbf{r}|$ (the ‘‘asymptotic solution’’), so that $\mathbf{r} - \mathbf{r}'$, $\mathbf{k}' := k' \hat{\mathbf{r}}$ and \mathbf{r} are parallel (see Fig. 2.1). Thus the approximation

$$|\mathbf{r} - \mathbf{r}'| = r - \frac{\mathbf{r}' \cdot \mathbf{k}'}{k'} \quad (2.15)$$

is valid and we obtain

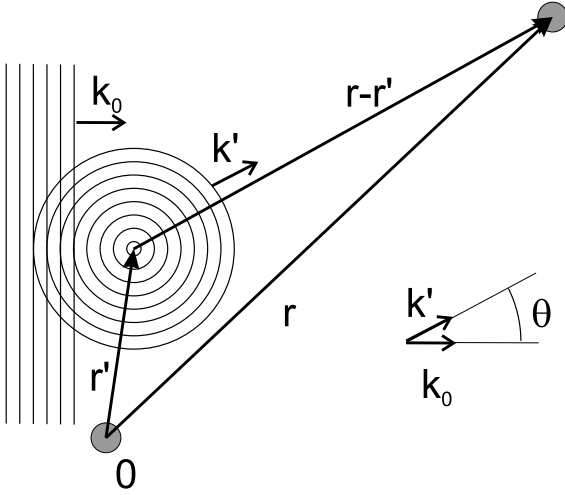


Fig. 2.1. Sketch showing an incident wave with wave vector \mathbf{k}_0 , scattered by a scattering center at \mathbf{r}' , which acts as a source of a secondary spherical wavelet $\Psi_1(\mathbf{r})$

$$\Psi_1(\mathbf{r}) = \sigma \exp(-2\pi i \mathbf{k}' \cdot \mathbf{r}) \int_{\Omega} \frac{\exp(-2\pi i (\mathbf{k}_0 - \mathbf{k}') \cdot \mathbf{r}')}{|\mathbf{r} - \mathbf{r}'|} \Phi(\mathbf{r}') d^3 \mathbf{r}' . \quad (2.16)$$

We now introduce the scattering vector $\mathbf{u} = -(\mathbf{k}_0 - \mathbf{k}')$, which is related to the scattering angle θ (see Fig. 2.1) by $u = (2/\lambda) \sin \theta/2$. Replacing $|\mathbf{r} - \mathbf{r}'|$ by r , we obtain:

$$\Psi(\mathbf{r}, \mathbf{u}) = \exp(-2\pi i \mathbf{k}_0 \cdot \mathbf{r}) + \frac{\exp(-2\pi i \mathbf{k}' \cdot \mathbf{r})}{r} f_e(\mathbf{u}) , \quad (2.17)$$

where $f_e(\mathbf{u})$ is the *atomic scattering factor for electrons*, given by

$$f_e(\mathbf{u}) = \sigma \int_{\Omega} \exp(2\pi i \mathbf{u} \cdot \mathbf{r}') \Phi(\mathbf{r}') d^3 \mathbf{r}' . \quad (2.18)$$

Note that $f_e(\mathbf{u})$ is also called the *scattering length* because it has dimensions of length. It is proportional to the Fourier transform of $\Phi(\mathbf{r})$, denoted by $\mathcal{F}\Phi(\mathbf{r})$ (see Sect. B.1). Equation (2.18) is analogous to the X-ray scattering factor

$$f_X(\mathbf{u}) = \int_{\Omega} \exp(2\pi i \mathbf{u} \cdot \mathbf{r}') n(\mathbf{r}') d^3 \mathbf{r}' , \quad (2.19)$$

where $n(\mathbf{r}')$ is the electron density distribution in the atom. Note that the electron is scattered by the Coulomb potential of the electron shell and the nucleus of the atom, whereas the X-ray scattering is due to the effect of the incident photon forcing an oscillation of the “hit” electron, which thus emits

a secondary wave. Poisson's equation provides a relation between the charge density of the electron shell and its contribution to the atomic potential. Values of $f_X(\mathbf{u})$ are available in the literature for most elements. The Mott formula

$$f_e(\mathbf{u}) = \frac{2\pi m e^2}{\epsilon_0 h^2} \frac{(Z - f_X(\mathbf{u}))}{|\mathbf{u}|^2}, \quad (2.20)$$

which is based on Poisson's equation, gives a relation between $f_e(\mathbf{u})$ and $f_X(\mathbf{u})$, where Z is the atomic number of the target atom and ϵ_0 the permittivity of a vacuum. Equation (2.20) has been used to compute $f_e(\mathbf{u})$ [4, 5]. A list of atomic scattering amplitudes $f_e(\mathbf{u})$ is provided in [5], and these are also used in the EMS program package [6]. There, the $f_e(\mathbf{u})$ are given for $m = m_0$ in the parametric form

$$f'_e(s) = \sum_{n=1}^4 a_n \exp(-b_n s^2), \quad \text{where } s = \frac{|u|}{2} = \frac{\sin(\theta/2)}{\lambda}. \quad (2.21)$$

Here a_n and b_n are the parameters listed in [5], given in units of \AA and \AA^2 , respectively. The relativistically corrected atomic scattering amplitudes are given by

$$f_e(\mathbf{u}) = \sqrt{\left(1 + \frac{h^2}{m_0^2 c^2 \lambda^2}\right)} f'_e\left(\frac{|\mathbf{u}|}{2}\right). \quad (2.22)$$

Figure 2.2 displays the atomic scattering amplitudes of Ga, In and As. One can clearly see that $f_e(\mathbf{u})$ depends on the type of scattering atom. This chemical sensitivity is the basis of the technique for compositional analysis described in this book. Figure 2.2 also reveals that the scattering amplitude decreases quickly with increasing scattering parameter $|\mathbf{u}|$.

2.2 Kinematical Approximation

2.2.1 The Structure Amplitude

The scattered electron wave function $\Psi_S(\mathbf{r}, \mathbf{u})$ is given in the first Born approximation (see (2.17)) by

$$\Psi_S(\mathbf{r}, \mathbf{u}) = \frac{\exp(-2\pi i k_0 r)}{r} f_e(\mathbf{u}). \quad (2.23)$$

We now consider a unit cell of a crystal containing N atoms with atomic scattering factors $f_e^{(i)}$ at positions \mathbf{r}_i ($i = 1, \dots, N$) (Fig. 2.3). We substitute $\mathbf{r}' = \mathbf{r}'' + \mathbf{r}_i$ in (2.18) and obtain the *structure amplitude* (also called the

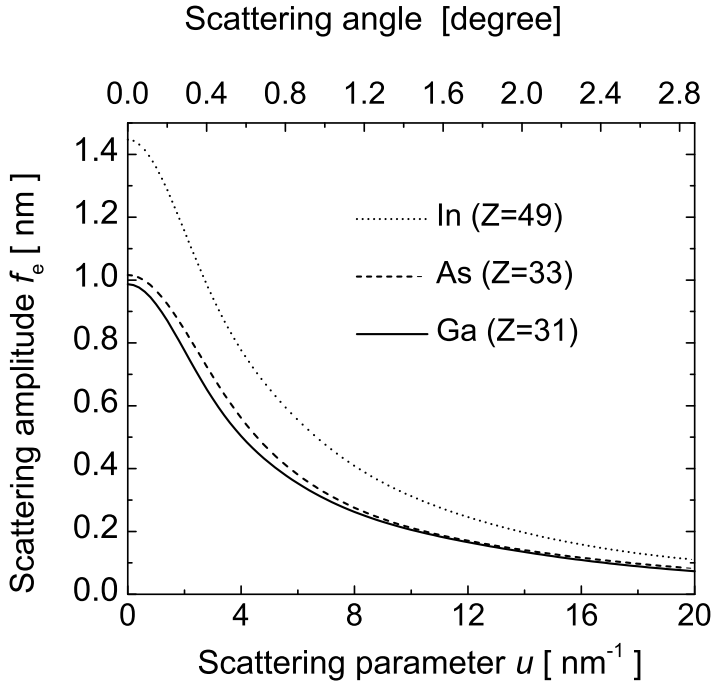


Fig. 2.2. Atomic scattering amplitudes for In, Ga and As plotted versus the scattering parameter $|\mathbf{u}|$, calculated for an accelerating voltage of 200 kV

structure factor) of the unit cell by summing the atomic scattering factors of all atoms in the unit cell according to

$$F_S(\mathbf{u}) = \sum_{i=1}^N \sigma \int \Phi^{(i)}(\mathbf{r}'') \exp \{2\pi i \mathbf{u} \cdot (\mathbf{r}'' + \mathbf{r}_i)\} d^3 \mathbf{r}'' \quad (2.24)$$

$$\Rightarrow F_S(\mathbf{u}) = \sum_{i=1}^N f_e^{(i)}(\mathbf{u}) \exp \{2\pi i (\mathbf{u} \cdot \mathbf{r}_i)\} . \quad (2.25)$$

2.2.2 The Lattice Amplitude

The interaction of the scattered waves emanating from a periodic assembly of unit cells leads to the effect of electron diffraction. Summing the structure amplitudes of unit cells with their origins at positions $\mathbf{r}_T = n_1 \mathbf{r}_1 + n_2 \mathbf{r}_2 + n_3 \mathbf{r}_3$, where $n_{1,2,3}$ are integers and $\mathbf{r}_{1,2,3}$ the lattice translation vectors, we obtain

$$G(\mathbf{u}) = F_S(\mathbf{u}) \sum_{n_{1,2,3}} \exp \{2\pi i [\mathbf{u} \cdot (n_1 \mathbf{r}_1 + n_2 \mathbf{r}_2 + n_3 \mathbf{r}_3)]\} \quad n_{1,2,3} \in \mathbb{N} . \quad (2.26)$$

Figure 2.4 clearly reveals that the modulus $|G(\mathbf{u})|$ is a peaked function, where each peak corresponds to a diffracted beam. Peaks occur for scattering vectors \mathbf{u} that obey

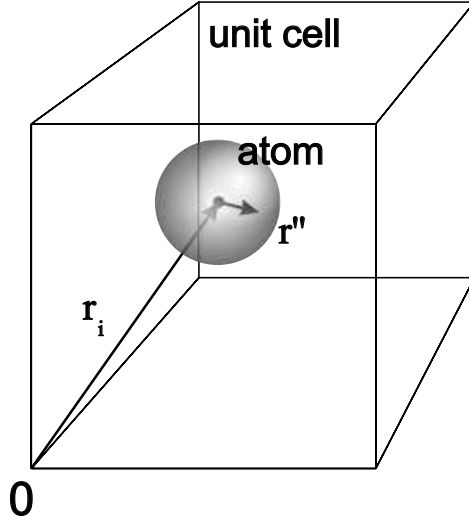


Fig. 2.3. Sketch of a unit cell, with the definition of the vectors \mathbf{r}_i and \mathbf{r}'' used in (2.24)

$$\mathbf{u} \cdot (n_1 \mathbf{r}_1 + n_2 \mathbf{r}_2 + n_3 \mathbf{r}_3) = n \quad n \in \mathbb{N}, \quad (2.27)$$

which is fulfilled when \mathbf{u} is a *reciprocal-lattice vector* \mathbf{g}_{hkl} with Miller indices h, k, l , such as

$$\mathbf{g}_{hkl} = h\mathbf{g}_1 + k\mathbf{g}_2 + l\mathbf{g}_3 \quad h, k, l \in \mathbb{N}. \quad (2.28)$$

The reciprocal-lattice base vectors $\mathbf{g}_{1,2,3}$ are defined by

$$\mathbf{g}_i = \frac{\mathbf{r}_j \times \mathbf{r}_k}{\mathbf{r}_i \cdot [\mathbf{r}_j \times \mathbf{r}_k]}, \quad (i, j, k) \in \{(1, 2, 3), (2, 3, 1), (3, 1, 2)\}. \quad (2.29)$$

We thus obtain for the vectors \mathbf{g}_{hkl}

$$\mathbf{g}_{hkl} \cdot (n_1 \mathbf{r}_1 + n_2 \mathbf{r}_2 + n_3 \mathbf{r}_3) = hn_1 + kn_2 + ln_3, \quad (2.30)$$

which proves that $\mathbf{u} = \mathbf{g}_{hkl}$ fulfills (2.27).

2.2.3 The Thin-Foil Specimen

To calculate the electron wave diffracted by a real specimen in the kinematical approximation, we consider a thin foil of thickness t . Summing the contributions from all points of the exit surface of the thin foil, interfering at a point P at a distance \mathbf{R} from the surface as displayed in Fig. 2.5, we obtain, for example from Fresnel's zone construction method [1], the total secondary wave corresponding to the diffraction vector \mathbf{g}_{hkl} as

$$\Psi_S(\mathbf{g}_{hkl}) = i\lambda t \frac{F_S(\mathbf{g}_{hkl})}{V_C} \exp\{-2\pi i \mathbf{k}_0 \cdot \mathbf{R}\}, \quad (2.31)$$

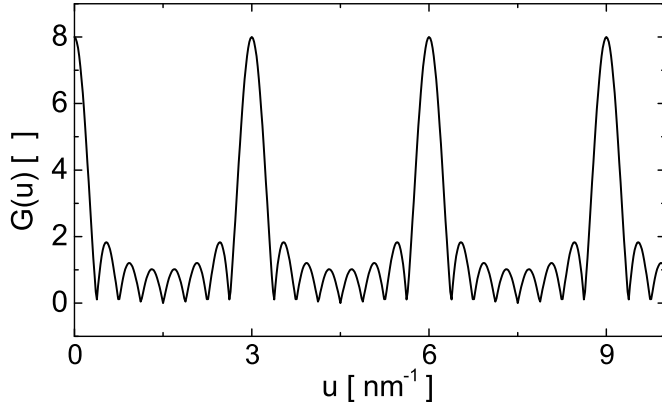


Fig. 2.4. Graph visualizing the effect of diffraction described by the lattice amplitude in (2.26). The function $|G(u)|$ is plotted versus the scattering “vector” u , where $G(u) = \sum_{n=0}^7 \exp\{2\pi i u (n r_1)\}$, using a 1D lattice translation “vector” $r_1 = (1/3)$ nm. Clearly, the modulus of $G(u)$ contains peaks at positions $u = 0, 3, 6, 9, \dots$, where $u r_1 = m$, $m \in \mathbb{N}$. The positions \mathbf{u} of the peaks correspond to the directions where constructive interference takes place, thus describing the propagation directions of diffracted beams

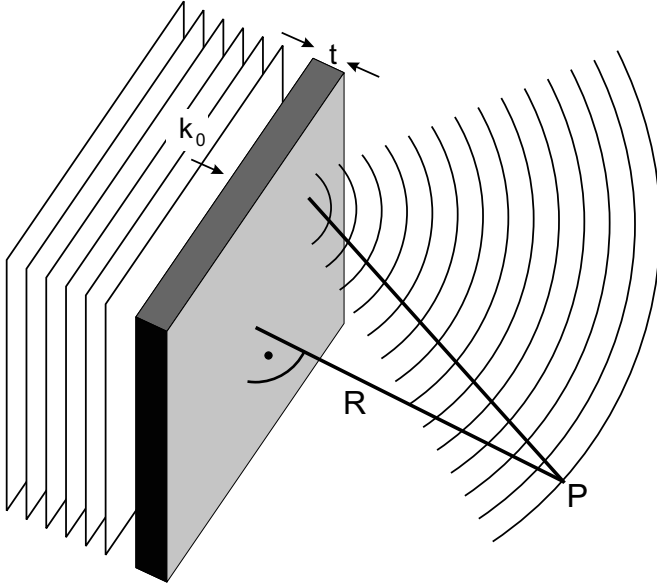


Fig. 2.5. An incident plane wave with wave vector \mathbf{k}_0 passing through a thin-foil specimen. At the point P , the wave function is composed of the sum of scattered waves from all points of the surface

where V_C is the volume of the unit cell. In the kinematical approximation, the amplitude of a diffracted beam \mathbf{g}_{hkl} increases linearly with the specimen thickness t . The dependence of the amplitude of the scattered wave upon $1/r$ that is obtained for single-atom scattering in (2.23) has vanished in (2.31). Note that if this approximation were valid, the the amplitude of the diffracted wave would become equal to the amplitude of the incident wave at $t_c = V_C / (F_S(\mathbf{g}_{hkl})\lambda)$ (e.g. $t_c = 15$ nm for \mathbf{g}_{002} in GaAs), whereas the

amplitude of the undiffracted beam would not change. This would violate energy conservation, and this consideration makes it clear that the kinematical approximation is valid only for a specimen thickness $t \ll t_c$.

In electron microscopy, the beams that contribute to the image are selected with the objective aperture, which is located in the back focal plane of the objective lens. The intensity of an image that is obtained in such a way that only the beam \mathbf{g}_{hkl} passes through the objective aperture, is given by

$$I(\mathbf{g}_{hkl}) = |\Psi_S(\mathbf{g}_{hkl})|^2 \propto |F_S(\mathbf{g}_{hkl})|^2 . \quad (2.32)$$

Such a micrograph is called a *single-beam bright-field* (BF) image if $\mathbf{g}_{hkl} = 0$ and a *single-beam dark-field* (DF) image otherwise. If more than one beam \mathbf{g}_{hkl} passes through the objective aperture, the electron waves of all beams interfere in the image plane, and nonlinear imaging theory must be applied to describe the intensity distribution.

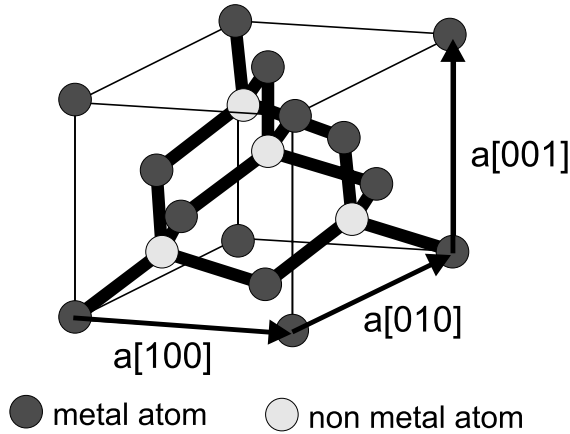


Fig. 2.6. The nonprimitive unit cell of the sphalerite crystal structure. The primitive basis vectors are $\mathbf{r}_1 = (a/2)[110]$, $\mathbf{r}_2 = (a/2)[101]$ and $\mathbf{r}_3 = (a/2)[011]$, where a is the lattice parameter. The basis contains two atoms of different type (metal or nonmetal) at positions \mathbf{r}_i and $\mathbf{r}_i + (1/4)a[111]$. By convention, the origin is occupied by a metal atom. The reciprocal-lattice base vectors are $\mathbf{g}_1 = a^{-1}[\bar{1}\bar{1}1]$, $\mathbf{g}_2 = a^{-1}[\bar{1}1\bar{1}]$ and $\mathbf{g}_3 = a^{-1}[1\bar{1}\bar{1}]$

2.2.4 Chemical Sensitivity

We now use the results of the preceding paragraphs to discuss chemical sensitivity in the kinematical approximation. Equation (2.31) shows that the amplitude of $\Psi_S(\mathbf{g}_{hkl})$ is proportional to $F_S(\mathbf{g}_{hkl})$. We therefore concentrate on the discussion of the structure factor. Since the present book is concerned with composition determination in sphalerite-type crystals (Fig. 2.6), we consider the structure factor of a beam \mathbf{g}_{hkl} for a binary material AC, given by